1032 *Chem. Mater.* **2011,** *23,* 1032–1038
DOI:10.1021/cm103068v

CHEMISTRY OF MATERIALS
Article

Template-Free Electrochemical Deposition of Interconnected ZnSb Nanoflakes for Li-Ion Battery Anodes

Somaye Saadat,[†] Yee Yan Tay,[†] Jixin Zhu,[†] Pei Fen Teh,[†] Saeed Maleksaeedi,[‡] Mohammad Mehdi Shahjamali,[†] Maziar Shakerzadeh,[§] Madhavi Srinivasan,[†,⊥] Bee Yen Tay,[‡] Huey Hoon Hng,[†] Jan Ma,[†] and Qingyu Yan*[,†,⊥]

[†]*School of Materials Science and Engineering, Nanyang Technological University, 50 Nanyang Avenue, Singapore 639798, Singapore,* [‡]*Singapore Institute of Manufacturing Technology, 71 Nanyang Drive, Singapore 638075, Singapore,* [§]*School of Electrical & Electronic Engineering, Nanyang Technological University, 50 Nanyang Avenue, Singapore 639798, Singapore, and* [⊥]*Energy Research Institute@NTU, Nanyang Technological University, Singapore 637459, Singapore*

Received October 26, 2010. Revised Manuscript Received December 21, 2010

A single-step fabrication of ZnSb nanostructures using template-free electrochemical deposition was developed. Results have indicated that ZnSb nanoflakes, nanowires, or nanoparticles with controlled composition could be obtained by adjusting the precursor concentration, applied voltage, and substrate type. The ZnSb nanostructures deposited on Cu foils were directly used as Li-ion battery anodes without the addition of any binder. Electrochemical analyses revealed that the interconnected ZnSb nanoflakes depicted high discharge capacities and a stable performance, which were better than that of ZnSb nanowires and nanoparticles. With an initial discharge capacity of 735 mA h/g and an initial Columbic efficiency of 85%, the ZnSb nanoflakes maintained a discharge capacity of 500 mA h/g with a Coulombic efficiency of 98% after 70 cycles at a current density of 100 mA/g (0.18 C). The ZnSb nanowires and nanoparticles showed a capacity of 190 and 40 mA h/g, respectively, after 70 cycles at the same current density. The improved performance of the interconnected ZnSb nanoflakes is attributed to their open structure, with a large surface area and small crystal grains, to facilitate the diffusion of Li ions and to buffer the large volume swings during the lithium intercalation process.

Introduction

Advances in rechargeable Li-ion batteries are promising to the development of portable electronics devices and hybrid electric vehicles.[1] Graphite and $LiCoO_2$ are currently used as electrode materials in commercial Li-ion secondary batteries. Graphite anodes with a theoretical capacity of 372 mA h/g have the advantages of flat charge and discharge curves, as well as excellent cyclability. However, since most lithium intercalation into graphite occurs at potentials of >100 mV versus Li^+/Li, this can result in the deposition of metallic lithium on the graphite surface during the fast charging/discharge processes, which gives rise to serious safety issues.[2,3] Thus, the search for alternative anode materials has been actively pursued.

Antimony alloys (e.g., Co−Sb,[4−6] Cu−Sb,[7] In−Sb,[8] Mn−Sb,[9] Cr−Sb,[10] and Zn−Sb[11−13]) have received great attention as promising anode materials, because of their high theoretical capacity and operating voltages that are higher than that of graphite, which is favorable for the improvement of battery safety. However, these alloys exhibit large structural strains and volume changes upon interacting with lithium, which can result in dramatic losses of capacity and poor charge/discharge cycling characteristics.[5,11,14]

*E-mail: alexyan@ntu.edu.sg.

(1) Tarascon, J. M.; Armand, M. *Nature* **2001**, *414*, 359–367.
(2) Fong, R.; von Sacken, U.; Dahn, J. R. *J. Electrochem. Soc.* **1990**, *137*, 2009–2013.
(3) Bruce, P. G.; Scrosati, B.; Tarascon, J. M. *Angew. Chem., Int. Ed.* **2008**, *47*, 2930–2946.
(4) Aicantara, R.; Fernandcz-Madrigal, F. J.; Lavcla, P.; Tirado, J. L.; Jumas, J. C.; Olivier-Fourcade, J. *J. Mater. Chem.* **1999**, *9*, 2517–2521.
(5) Ionica, C. M.; Lippens, P. E.; Fourcade, J. O.; Jumas, J. C. *J. Power Sources* **2005**, *146*, 478–481.
(6) Zhu, J.; Sun, T.; Chen, J.; Shi, W.; Zhang, X.; Lou, X.; Mhaisalkar, S.; Hng, H. H.; Boey, F.; Ma, J.; Yan, Q. *Chem. Mater.* **2010**, *22*, 5333–5339.
(7) Fransson, L. M. L.; Vaughey, J. T.; Benedek, R.; Edström, K.; Thomas, J. O.; Thackeray, M. M. *Electrochem. Commun.* **2001**, *3*, 317–323.
(8) Kropf, A. J.; Tostmann, H.; Johnson, C. S.; Vaughey, J. T.; Thackeray, M. M. *Electrochem. Commun.* **2001**, *3*, 244–251.
(9) Fransson, L. M. L.; Vaughey, J. T.; EdstrÖm, K.; Thackeray, M. M. *J. Electrochem. Soc.* **2003**, *150*, A86–A91.
(10) Fernández-Madrigal, F. J.; Lavela, P.; Pérez-Vicente, C.; Tirado, J. L. *J. Electroanal. Chem.* **2001**, *501*, 205–209.
(11) Zhao, X. B.; Cao, G. S. *Electrochim. Acta* **2001**, *46*, 891–896.
(12) Lu, C. P.; Zhao, X. B.; Cao, G. S.; Zhu, T. J. *Trans. Nonferrous Met. Soc. China* **2000**, *10*, 204–208.
(13) Park, C. M.; Sohn, H. J. *Adv. Mater.* **2010**, *22*, 47–52.
(14) Winter, M.; Besenhard, J. O.; Spahr, M. E.; Novák, P. *Adv. Mater.* **1998**, *10*, 725–763.

Published on Web 01/07/2011

Nanostructured electrode materials have been considered as one promising direction to improve the performance of Li-ion secondary batteries, because of their large surface-to-volume ratio and short diffusion distance for lithium alloying or intercalation.[3,15−18] Furthermore, hollow and porous nanostructures are shown to be beneficial to partially buffer the large volume swing during lithiation, to improve the charge/discharge cycling performance.[3,17,19−23] Currently, the general preparation of nanostructured battery electrodes is to add a binder (e.g., poly(vinylidene difluoride)) and paste onto the current collectors. In most cases, a conductive agent (e.g., carbon black) also must be added, to improve the electrical conductivity. This process essentially adds extra weight to the electrodes, which will decrease the overall charge capacity of the electrodes. In fact, many reports only take the weight of the active nanostructures into account during the evaluation of the charge capacities of electrode materials, to show the promising electrochemical performance.

The direct deposition of active materials onto current collector by electrochemical techniques is an encouraging approach, since it does not require any binding or pasting process.[24−27] However, preparing nanostructures using electrochemical deposition normally require hard templates (e.g., anodized aluminum oxides to fabricate nanowires[28,29]) or polystyrene spheres (to prepare porous structures[30]). These processes require removal of the templates, and there is a high possibility that the impurities from the template materials can still remain in the nanostructures, which will affect the charge capacity. Herein, we report a template-free single-step synthesis process to prepare nanoporous structures of interconnected ZnSb nanoflakes on Cu substrates by electrochemical deposition. By varying the deposition parameters (e.g., deposition voltage, molar ratio between precursors of Zn and Sb, and substrate roughness), Zn−Sb nanoflakes, nanowires, or nanoparticles can be prepared with tunable Zn:Sb molar ratios. Furthermore, these ZnSb nanostructures were tested as Li-ion battery anodes. Comparison with that of ZnSb nanoparticles and nanowires showed improved electrochemical performance for the interconnected ZnSb nanoflakes (e.g., a discharge capacity of 500 mA h/g with 98% Coulombic efficiency was achieved after 70 cycles at a current density of 100 mA/g (0.18 C)).

Experimental Section

Electrochemical Deposition of ZnSb. The electrochemical depositions were carried out in a three-electrode cell using a potentiostat/galvanostat instrument (CH Instruments, Model 1200A). The working electrodes were two types of smooth and rough high-purity copper foil (99.99%). Before electrodeposition, the copper substrate was rinsed with distilled water, and acetone carefully to remove any impurities. A platinum wire with the diameter of 0.5 mm was used as a counter electrode and an Ag/AgCl electrode was used as the reference. The distance between the working and counter electrodes was fixed at 2.0 cm. The bath was filled with ethylene glycol (99.5 purity, Sigma−Aldrich) that contained $ZnCl_2$ (99.5 purity, Sigma−Aldrich) and $SbCl_3$ (99.95 purity, Sigma−Aldrich).

Constant potentials in the range of 3−9 V were applied for electrochemical deposition. Electrochemical deposition process was performed at room temperature without any stirring or inert-gas bubbling. After deposition, the electrodes were rinsed with ethanol several times and then dried in a vacuum oven for 6 h.

Characterization. The sample morphology was examined using transmission electron microscopy (TEM) (JEOL, Model JEM-2100) and field-emission scanning electron microscopy (FESEM) (JEOL, Model JSM-7600F). The elemental compositions of the samples were analyzed with an energy-dispersive X-ray spectroscopy (EDX) system that was attached to the TEM equipment. Crystallographic information for the samples was collected using powder X-ray diffraction (XRD) (Bruker AXS, Model D8 advance, Cu Kα radiation with $\lambda = 1.5406$ Å).

Electrochemical Measurements. For the electrochemical measurement, a thin carbon layer (10 nm) was deposited on the as-prepared ZnSb samples, using a double-bend filtered cathodic vacuum arc (FCVA). A negative substrate bias of 200 V was applied to the substrate during the deposition.

Assembly of the coin-type battery cells was performed in an argon-filled glovebox with < 1.00 ppm of moisture and oxygen. The working electrode was a ZnSb nanostructure on copper foil without the addition of any binder. Lithium foil was used both as the counter electrode and reference electrode, while 1 M $LiPF_6$ in ethylene carbonate (EC)/diethyl carbonate (DEC) (1:1 by volume) was used as the electrolyte. All the coin cells were tested galvanostatically between 0.0 V and 2.0 V (vs Li/Li^+) at a current density of 100 mA/g (0.18 C), using a NEWWARE battery tester.

(15) Derrien, G.; Hassoun, J.; Panero, S.; Scrosati, B. *Adv. Mater.* **2007**, *19*, 2336–2340.
(16) Aricò, A. S.; Bruce, P.; Scrosati, B.; Tarascon, J. M.; Van Schalkwijk, W. *Nat. Mater.* **2005**, *4*, 366–377.
(17) Guo, Y. G.; Hu, J. S.; Wan, L. J. *Adv. Mater.* **2008**, *20*, 2878–2887.
(18) Wang, W.; Kumta, P. N. *ACS Nano* **2010**, *4*, 2233–2241.
(19) Lou, X. W.; Deng, D.; Lee, J. Y.; Archer, L. A. *Chem. Mater.* **2008**, *20*, 6562–6566.
(20) Kim, S. W.; Kim, M.; Lee, W. Y.; Hyeon, T. *J. Am. Chem. Soc.* **2002**, *124*, 7642–7643.
(21) Yang, L. C.; Gao, Q. S.; Li, L.; Tang, Y.; Wu, Y. P. *Electrochem. Commun.* **2010**, *12*, 418–421.
(22) Liu, D.; Garcia, B. B.; Zhang, Q.; Guo, Q.; Zhang, Y.; Sepehri, S.; Cao, G. *Adv. Funct. Mater.* **2009**, *19*, 1015–1023.
(23) Liu, P.; Lee, S. H.; Tracy, C. E.; Yan, Y.; Turner, J. A. *Adv. Mater.* **2002**, *14*, 27–30.
(24) Shin, H. C.; Dong, J.; Liu, M. *Adv. Mater.* **2003**, *15*, 1610–1614.
(25) Hu, C. C.; Huang, Y. H. *J. Am. Chem. Soc.* **1999**, *146*, 2465–2471.
(26) Tamura, N.; Ohshita, R.; Fujimoto, M.; Fujitani, S.; Kamino, M.; Yonezu, I. *J. Power Sources* **2002**, *107*, 48–55.
(27) Taberna, P. L.; Mitra, S.; Poizot, P.; Simon, P.; Tarascon, J. M. *Nat. Mater.* **2006**, *5*, 567–573.
(28) Duan, H.; Gnanaraj, J.; Chen, X.; Li, B.; Liang, J. *J. Power Sources.* **2008**, *185*, 512–518.
(29) Chou, S.; Cheng, F.; Chen, J. *Eur. J. Inorg. Chem.* **2005**, *2005*, 4035–4039.
(30) Bartlett, P. N.; Baumberg, J. J.; Birkin, P. R.; Ghanem, M. A.; Netti, M. C. *Chem. Mater.* **2002**, *14*, 2199–2208.

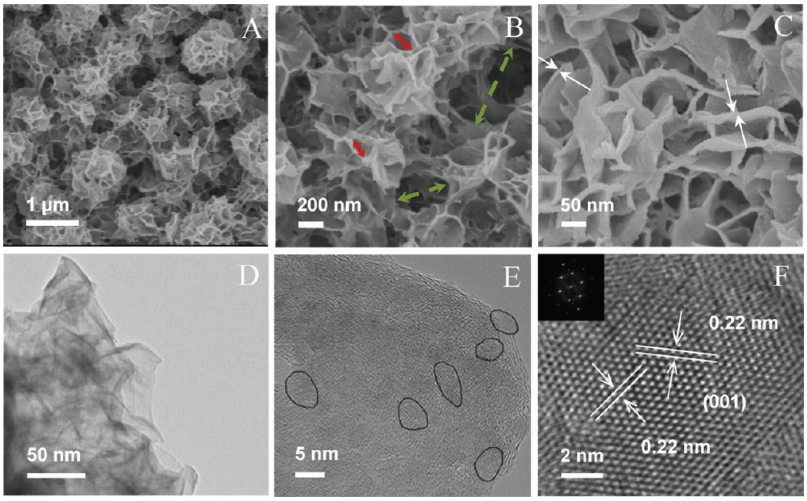

Figure 1. (A, B, C) SEM images, (D) TEM image, and (E,F) HRTEM images of ZnSb nanoflakes electrodeposited in an ethylene glycol solution with a precursor molar ratio of $I_{ZnCl_2-SbCl_3} = 1.6$ and an applied voltage of $V_d = -7$ V for 200 s on smooth copper. Although the nanoflakes are polycrystalline, as indicated by the circles in panel E, most of the grains show a preferred exposure of (001) facets on the surface of the nanoflakes (also see Figure S2 in the Supporting Information).

Results and Discussion

To monitor the electrochemical deposition of Zn and Sb ions in ethylene glycol, a cyclic voltammogram (CV) study was performed on copper electrodes in an ethylene glycol solution that contained 0.05 mol/L $ZnCl_2$ and 0.03 mol/L $SbCl_3$ under ambient conditions. Two cathodic peaks were observed, at −0.9 V and −2.25 V in the CV curve (see Figure S1 in the Supporting Information), corresponding to the electrochemical reduction of Sb and Zn, respectively.

Figure 1 shows scanning electron microscopy (SEM) and TEM images of Zn−Sb alloys grown on smooth copper foils from the above-mentioned electrolyte under a deposition voltage of $V_d = -7$ V for 200 s. It reveals that the as-deposited Zn−Sb alloy formed porous structures that were composed of interconnected nanoflakes under such an overpotential process (see Figure 1A). The pore size between the flakes was in a wide range (100−800 nm), as shown in Figure 1B. The thickness of the nanoflakes was 10−20 nm (see Figure 1C). The TEM image, as shown in Figure 1D, demonstrates that part of the porous Zn−Sb alloy was composed of thin flakes, which appeared translucent and were spread in different directions. The average atomic ratio of the ZnSb nanoflakes was Zn:Sb ≈ 51:49, as revealed by the EDX analysis in the TEM system. The high-resolution transmission electron microscopy (HRTEM) observation (see Figure 1E) of the Zn−Sb nanoflakes indicates that they were polycrystalline with a grain size in the range of 5−10 nm. It was also observed that the lattices that were present had an equal interfringe spacing of 0.22 nm, corresponding to the (110) plane (Figure 1F) of the hexagonal ZnSb phase (Joint Committee on Powder Diffraction Standards (JCPDS) File Card No. 18-0140). The fast Fourier transform (FFT) pattern of the same region (Figure 1F) was indexed to the diffraction spots of the [001] zone. As revealed by our HRTEM observation (see Figure S2 in the Supporting Information), there was a large portion of the ZnSb nanocrystals in the flakes showing preferred exposure of the (001) facets, although there were still some ZnSb nanocrystals showing other orientations. The XRD pattern of the as-prepared flakes (see Figure 2) confirmed the formation of the hexagonal ZnSb (JCPDS File Card No. 18-0140), which is consistent with the HRTEM observation.

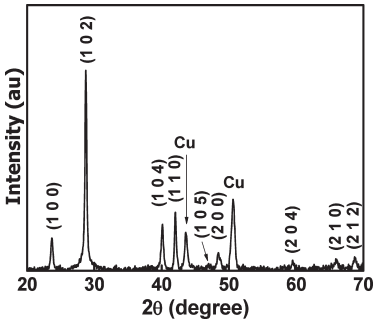

Figure 2. XRD pattern of ZnSb nanoflakes electrodeposited in ethylene glycol solution with $I_{ZnCl_2-SbCl_3} = 1.6$ and $V_d = -7$ V for 200 s on smooth copper.

To control the composition of the Zn−Sb nanoflakes under such an overpotential process, deposition processes were also carried out, using electrolytes with different precursor ratios. The effect of the precursor molar ratio (e.g., $I_{ZnCl_2-SbCl_3}$ = $ZnCl_2$:$SbCl_3$) on the morphology of the Zn−Sb nanostructures was investigated (see Figures 3A−C). Under the same deposition conditions (e.g., $V_d = -7$ V for 200 s), varying $I_{ZnCl_2-SbCl_3}$ from 1.6 to 2.0 and 2.4 resulted in interconnected nanoflakes each time. The morphologies of the Zn−Sb deposits were similar, while the sizes of the flakes varied. For example, the nanoflakes deposited with $I_{ZnCl_2-SbCl_3} = 1.6$ had a width of 100−200 nm, which increased to 300−400 nm for samples deposited with $I_{ZnCl_2-SbCl_3} = 2.4$. Although the morphologies of the Zn−Sb nanoflakes deposited with different $I_{ZnCl_2-SbCl_3}$ values were similar, the Zn:Sb ratios of the

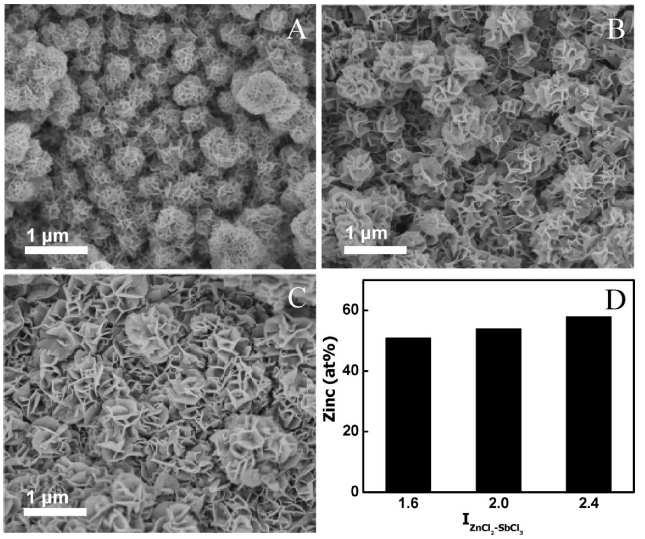

Figure 3. SEM images of nanoflake Zn−Sb alloy deposited in ethylene glycol solution with precursor molar ratios of (A) $I_{ZnCl_2-SbCl_3} = 1.6$, (B) $I_{ZnCl_2-SbCl_3} = 2$, (C) $I_{ZnCl_2-SbCl_3} = 2.4$ and $V_d = -7$ V for 200 s on smooth copper, (D) zinc atomic percentage in the nanoflake Zn−Sb alloy deposited with different $I_{ZnCl_2-SbCl_3}$ values.

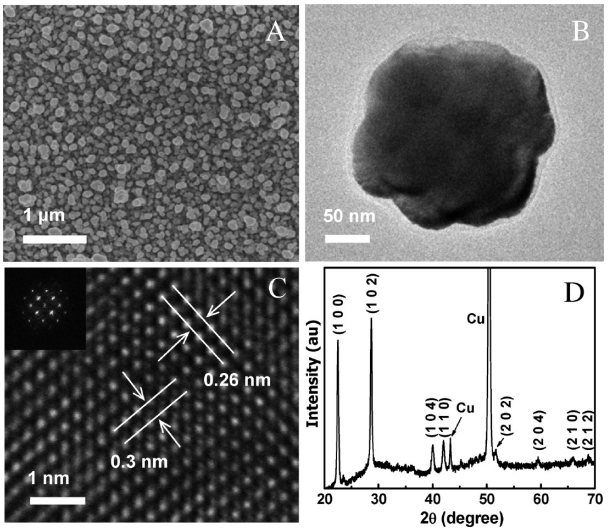

Figure 4. (A) Scanning electron microscopy (SEM) image, (B) transmission electron microscopy (TEM) image, (C) high-resolution transmission electron microscopy (HRTEM) image, and (D) X-ray diffraction (XRD) pattern of ZnSb nanoparticles deposited in an ethylene glycol solution with a precursor ratio of $I_{ZnCl_2-SbCl_3} = 2$ and an applied voltage of $V_d = -3$ V for 200 s on smooth copper.

samples were different, as revealed by EDX spectroscopy in the TEM analysis; the ratios are presented in Figure 3D. It is reasonable to deduce that higher values of $I_{ZnCl_2-SbCl_3}$ led to increased amount of zinc in the as-deposited nanoflakes. Meanwhile, the change of the composition of the nanoflakes also resulted in the formation of other impurity phases (see Figure S3 in the Supporting Information).

The effects of other parameters (e.g., deposition voltage and substrate roughness) on the growth of Zn−Sb alloys were also investigated. It was found that decreased deposition voltage led to the formation of nanoparticles. For example, ZnSb nanoparticles were formed with $I_{ZnCl_2-SbCl_3} = 2$ and $V_d = -3$ V on smooth copper substrate (see Figures 4A and 4B). The particle size was in the range of 60−120 nm, with an average atomic ratio of Zn:Sb = 48:52. The XRD pattern confirmed the formation of the hexagonal ZnSb (JCPDS File Card No. 18-0140) and no additional peaks from impurity phases were observed (see Figure 4D). HRTEM observation (see Figure 4C) of the Zn−Sb nanoparticles indicated two perpendicular planes with interfringe spacings of 0.26 and 0.3 nm, corresponding to the (103) and (102) planes of the hexagonal ZnSb phase (JCPDS File Card No. 18-0140), respectively. To investigate the influence of substrate morphology, rough copper foils with an average surface roughness (R_a) of 268 nm (see Figure S4A in the Supporting Information) was used, instead of smooth copper foils with $R_a = 66$ nm (see Figure S4B in the Supporting Information). Interestingly, growth of the ZnSb nanowires (see Figure 5A and 5B) were observed in the solution with $I_{ZnCl_2-SbCl_3} = 1.6$ and $V_d = -9$ V. The diameter and length of these ZnSb nanowires were in the ranges of 70−150 nm and 1−1.5 μm, respectively. The average atomic ratio, as examined by TEM, was Zn:Sb = 51:49. Similarly, only hexagonal ZnSb (JCPDS File Card

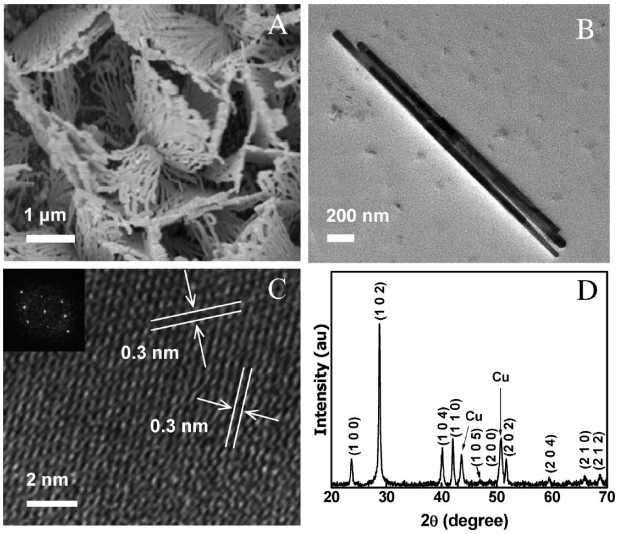

Figure 5. (A) SEM, (B) TEM, (C) HRTEM, and (D) XRD pattern of ZnSb nanowires deposited in an ethylene glycol solution with a precursor ratio of $I_{ZnCl_2-SbCl_3} = 1.6$ and an applied voltage of $V_d = -9$ V for 200 s on rough copper.

No. 18-0140) was detected using XRD (see Figure 5D). HRTEM observation (see Figure 5C) of the Zn−Sb nanowires indicated that the present lattices had an equal interfringe spacing of 0.3 nm, corresponding to the (102) plane (see Figure 5D) of the hexagonal ZnSb phase (JCPDS File Card No. 18-0140). A more complete processing-related growth of the Zn−Sb alloy nanostructures was investigated for various processing parameters. It was indicated that, similar to that observed for the deposition of the nanoflakes, varying the $I_{ZnCl_2-SbCl_3}$ values led to the formation of impurity phases, because of the change in the Zn:Sb ratio.

The above observation indicates that the growth of ZnSb nanoflakes is closely related to the fast nucleation

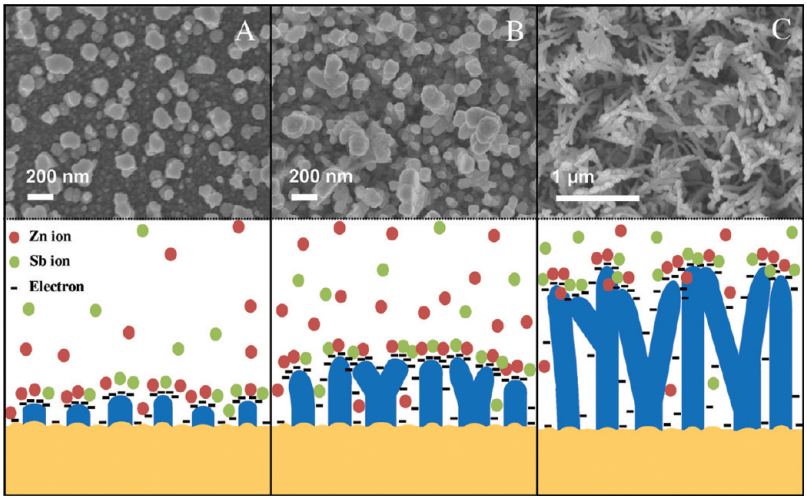

Figure 6. SEM images and schematic drawing of the deposition of ZnSb nanowires on rough copper in an ethylene glycol solution with a precursor molar ratio of $I_{ZnCl_2-SbCl_3} = 1.6$ and an applied voltage of $V_d = -9$ V for different times ((A) 15 s, (B) 25 s, and (C) 200 s).

and growth process induced by the high applied overvoltage. On the other hand, the growth of ZnSb nanoparticles formed under lower deposition voltage is possibly related to the diffusion of as-deposited Zn/Sb atoms on the ZnSb nucleus to reduce the total surface area, which, in turn, decreases the surface energy. For materials with a hexagonal symmetric lattice, it is well-reported that flake or disk-shaped nanostructures can be formed by various synthesis techniques.[31,32] The growth of single-crystalline Sb_2Te_3 nanoplates with hexagonal crystals lattice has been demonstrated.[31,33] Such growth is mainly controlled by the intrinsic crystal structure, similar to that observed for the growth of ZnSb nanoflakes. It is possible that the formation of nanoflakes, during such a fast nucleation and growth process under an applied voltage of −7 V, is due to the confined growth within the (001) planes. The polycrystalline nature of the ZnSb is possibly due to the fast growth process, which may lead to the generation of structural defects and, in turn, form grain boundaries. Other possibilities also may exist (e.g., the template effect from the gas bubbles generated, which can lead to the formation of interconnected flakes).[34,35] The growth of the ZnSb nanowires is mainly attributed to the seeding effect from the substrates. Based on SEM observation during the first 15 s, short rods 100−150 nm in length started to grow from the rough substrates (see Figure 6A). After 25 s, the rods grew longer and the number of rods also increased (see Figure 6B); finally, after 200 s, the ZnSb grew into nanowires with a length of 1−1.5 μm, which were partially branched (see Figure 6C). Since the deposition condition of nanowires was the same as that used to fabricate ZnSb nanoflakes on smooth copper, it can be concluded that the formation of wires is due to the substrate effect. The proposed growth mechanism for this case is related to the convex locations of the rough foils that have higher concentration of electrons (to significantly attract metallic ions and to serve as seeds for local nucleation of ZnSb) and limits the one-dimensional growth of ZnSb (see scheme presented in Figure 6).

To study the Li-ion storage capabilities of the ZnSb nanostructures, a series of electrochemical measurements were carried out based on the half-cell configuration.[36,37] Here, the as-deposited ZnSb on copper foils were directly used as the anodes without the addition of any binder. A 10-nm-thick amorphous carbon layer was deposited on top of the ZnSb samples, which may improve the lithium storage performance.[38,39] Figure 7A displays the cyclic voltammograms (CVs) of the first and second cycles of ZnSb nanoflakes deposited with $I_{ZnCl_2-SbCl_3} = 1.6$ and $V_d = -7$ V, obtained at a scan rate of 0.5 mV/s. The observed redox peaks in the charge and discharge cycles were consistent with those previously reported for ZnSb.[13] The different phases, which appeared at different voltages, are labeled in Figure 7A, and they correspond to the following steps:[13]

1st Cycle:

$$ZnSb \xrightarrow{A} LiZnSb \xrightarrow{B} Li_3Sb + Zn \xrightarrow{C} Li_3Sb + LiZn$$

$$Li_3Sb + LiZn \xrightarrow{D}$$

$$Li_3Sb + Zn \xrightarrow{E} Li_2ZnSb \xrightarrow{F} Li_{2-x-}ZnSb \qquad (0 \le x \le 2)$$

(31) Shi, W. D.; Zhou, L.; Song, S. Y.; Yang, J. H.; Zhang, H. J. *Adv. Mater.* **2008**, *20*, 1892–1897.
(32) Zhang, X.; Shi, W.; Zhu, J.; Zhao, W.; Ma, J.; Mhaisalkar, S.; Maria, T.; Yang, Y.; Zhang, H.; Hng, H.; Yan, Q. *Nano Res.* **2010**, *3*, 643–652.
(33) Wang, W. Z.; Poudel, B.; Yang, J.; Wang, D. Z.; Ren, Z. F. *J. Am. Chem. Soc.* **2005**, *127*, 13792–13793.
(34) Xiao, W.; Xia, H.; Fuh, J. Y. H.; Lu, L. *J. Electrochem. Soc.* **2009**, *156*, A627–A633.
(35) Zhang, L.; Zhang, Y.; Zhang, X.; Li, Z.; Shen, G.; Ye, M.; Fan, C.; Fang, H.; Hu, J. *Langmuir* **2006**, *22*, 8109–8113.
(36) Wang, D. H.; Choi, D. W.; Li, J.; Yang, Z. G.; Nie, Z. M.; Kou, R.; Hu, D. H.; Wang, C. M.; Saraf, L. V.; Zhang, J. G.; Aksay, I. A.; Liu, J. *ACS Nano* **2009**, *3*, 907–914.
(37) Wang, D. H.; Kou, R.; Choi, D.; Yang, Z. G.; Nie, Z. M.; Li, J.; Saraf, L. V.; Hu, D. H.; Zhang, J. G.; Graff, G. L.; Liu, J.; Pope, M. A.; Aksay, I. A. *ACS Nano* **2010**, *4*, 1587–1595.
(38) Kim, H.; Cho, J. *J. Electrochem. Soc.* **2007**, *154*, A462–A466.
(39) Kwon, Y.; Kim, H.; Doo, S.-G.; Cho, J. *Chem. Mater.* **2007**, *19*, 982–986.

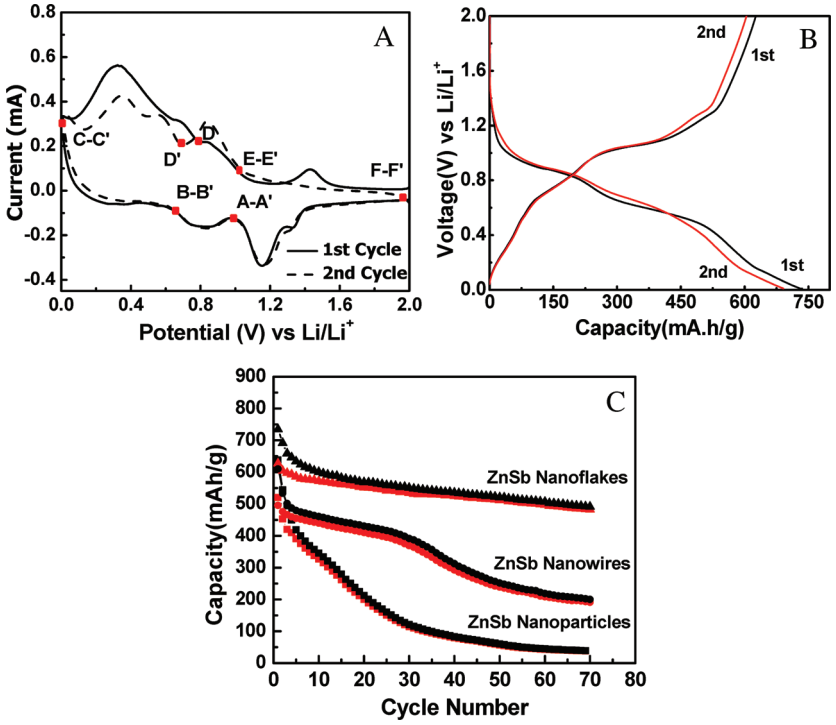

Figure 7. (A) Cyclic voltammograms (CVs) of the first and second cycles of ZnSb nanoflakes obtained with $I_{ZnCl_2-SbCl_3} = 1.6$ and $V_d = -7$ V at a scan rate of 0.5 mv/s. (B) Charge/discharge voltage profiles of ZnSb nanoflakes between 0 and 2 V (vs Li/Li^+) at a current density of 100 mA/g (0.18 C). (C) Charge/discharge cycling performance of ZnSb nanoflakes, nanowires, and nanoparticles between 0 V and 2 V (vs Li/Li^+) at a current density of 100 mA/g (0.18 C).

2nd Cycle:

$$Li_{2-x}ZnSb \xrightarrow{A'} LiZnSb \xrightarrow{B'} Li_3Sb + Zn \xrightarrow{C'} Li_3Sb + LiZn$$

$$Li_3Sb + LiZn \xrightarrow{D'} Li_3Sb + Zn \xrightarrow{E'} Li_2ZnSb \xrightarrow{F'} Li_{2-x-}ZnSb \qquad (0 \le x \le 2)$$

Figure 7B showed the corresponding charge/discharge voltage profiles of the same ZnSb nanoflakes at a current density of 100 mA/g (0.18 C). The potential plateaus observed the discharge curves were consistent with the CV results. The insertion process gave a first discharge capacity of 735 mA h/g and a subsequent charge capacity of 627 mA h/g, resulting in an initial Coulombic efficiency of 85%. During the second cycle, the discharge capacity decreased to 691 mA h/g, with a corresponding charge capacity of 604 mA h/g, leading to a higher Coulombic efficiency of 87%. Here, for all the capacity measurements, the total weight of the active materials was considered (e.g., ZnSb + amorphous carbon layer). The charge/discharge cycling performance of the ZnSb nanoflakes was evaluated between 0 V and 2.0 V at 0.18 C (see Figure 7C). With an initial discharge capacity of 735 mA h/g, the ZnSb nanoflakes maintained a discharge capacity of 500 mA h/g, with a Coulombic efficiency of 98% after 70 cycles, which was greater than that of a commercially used graphite anode (e.g., 372 mA h/g). As a comparison, the same test was carried out on carbon-coated ZnSb nanoparticles and nanowires with similar composition and phase (e.g., nanoparticles deposited with $I_{ZnCl_2-SbCl_3} = 2.0$ and $V_d = -3$ V on smooth Cu), as shown in Figures 4A and 4B and nanowires deposited with $I_{ZnCl_2-SbCl_3} = 1.6$ and $V_d = -9$ V on rough copper, as shown in Figures 5A and 5B. Both ZnSb nanoparticles and nanowires showed worse battery-electrode performances, compared to that of ZnSb nanoflakes (see Figure 7C). The ZnSb nanoparticles showed a lower initial discharge capacity of 638 mA h/g, which decreased rapidly to 544 mA h/g in the second cycle and to < 100 mA h/g after 70 cycles. ZnSb nanowires showed a first-cycle discharge capacity of 610 mA h/g, which decreased to 190 mA h/g after 70 cycles. To demonstrate the influence of carbon coating on battery performance, the pure ZnSb nanoparticles, nanowires, and nanoflakes electrodes with no carbon coating were assembled into coin cells and their electrochemical performance were analyzed. The higher initial capacities obtained in the ZnSb nanoflakes, compared to that of nanoparticles and nanowires, were possibly due to their open structure and the thinness was needed to facilitate the access and diffusion of Li ions. The stable cycling performance of the nanoflakes was attributed to be related to such porous structures that can buffer the large strain that is induced by the volume swing during the lithiation process. We also noted that the presence of the thin carbon coating was very important to improve the cycling performance of the ZnSb nanostructures; without the carbon coating, the capacity retention of the ZnSb nanostructures was much worse (see Figure S5 in the Supporting Information).

Conclusion

Interconnected ZnSb nanoflakes were prepared by a template-free electrochemical deposition process under high overpotential conditions. The composition and morphology of the ZnSb nanostructures could be tuned by varying the molar ratio of the precursors (e.g., $ZnCl_2$:$SbCl_3$), the deposition potentials, and the substrate roughness. The ZnSb nanostructures on copper substrates could be directly used as Li-ion battery anodes without the addition of any binder. The electrochemical tests revealed that the ZnSb nanoflakes showed high Li-ion storage capacities and stable cyclabilities (e.g., a discharge capacity of 500 mA h/g was maintained after 70 cycles, with a Coulombic efficiency of 98%). For comparison, ZnSb nanoparticles and nanowires with similar compositions and phase were electrochemically tested, and these showed lower discharge capacities and worse cycling stabilities. The better performance of the ZnSb flakes was mainly attributed to their open porous structure and thinness, which facilitated the Li-ion access and diffusion, and buffered the induced strain by the volume expansion during the lithiation process. Such synthesis approach of interconnected ZnSb nanoflakes may be applied onto other promising materials for energy storage applications, such as electrodes for Li-ion batteries or supercapacitors.

Acknowledgment. The authors gratefully acknowledge AcRF Tier 1 RG 31/08 of MOE (Singapore), NRF2009EWT-CERP001-026 (Singapore), AcRF Tier 2 (MOE2010-T2-1-017), NRF2009EWT-CERP001-036, (Singapore).

Supporting Information Available: Voltammogram study of Zn−Sb−ethylene glycol solution (Figure S1), HRTEM images (Figure S2), XRD pattern (Figure S3), surface roughness profile (Figure S4) of substrates and the electrochemical performance of pure ZnSb nanostructures (Figure S5). This material is available free of charge via the Internet at http://pubs.acs.org.